Advances in Geosciences
Vol. 10: Atmospheric Science (2007)
Eds. J. H. Oh and G. P. Singh

FORMATION OF TROPICAL CYCLONE CONCENTRIC EYEWALLS BY WAVE–MEAN FLOW INTERACTIONS

JIAYI PENG
International Pacific Research Center, University of Hawaii,
1680 East West Road, Honolulu, Hawaii, USA

TIM LI
Department of Meteorology and International Pacific Research Center,
School of Ocean and Earth Science and Technology,
University of Hawaii, Honolulu, Hawaii, USA

MELINDA S. PENG
Naval Research Laboratory, Monterey, California, USA

The role of two-way interactions between a symmetric core vortex and an asymmetric disturbance in generating tropical cyclone (TC) concentric eyewalls is examined in a nonlinear barotropic model. The results show that when an asymmetric perturbation is placed outside of the radius of maximum wind, an asymmetric disturbance develops in the inner region, resulting in a weakening of the symmetric flow *in situ*, while the symmetric tangential wind gains energy from the asymmetric perturbations in the outer region. This process leads double peaks in the symmetric tangential wind profile. Further diagnosis reveals that the distinctive evolution features in the inner and outer regions are determined by the asymmetric up- (down-) shear tilting structure and so-induced symmetry-to-asymmetry (asymmetry-to-symmetry) energy transfer. There exists an optimal radius location for the initial perturbation to generate most efficiently a double-peak structure in the symmetric tangential wind profile.

1. Introduction

Concentric eyewalls have been observed in the life cycle of strong tropical cyclones (TC). Willoughby *et al.*[12] identified a double eyewall structure for hurricane Gilbert with the inner eyewall in the radius of 8–20 km and the outer eyewall between 55 and 100 km. A more detailed analysis of Gilbert[1] showed that the primary eyewall appeared first. During a weakening stage of the storm, the outer eyewall formed. Later on, the outer eyewall strengthened and contracted while the inner eyewall weakened.

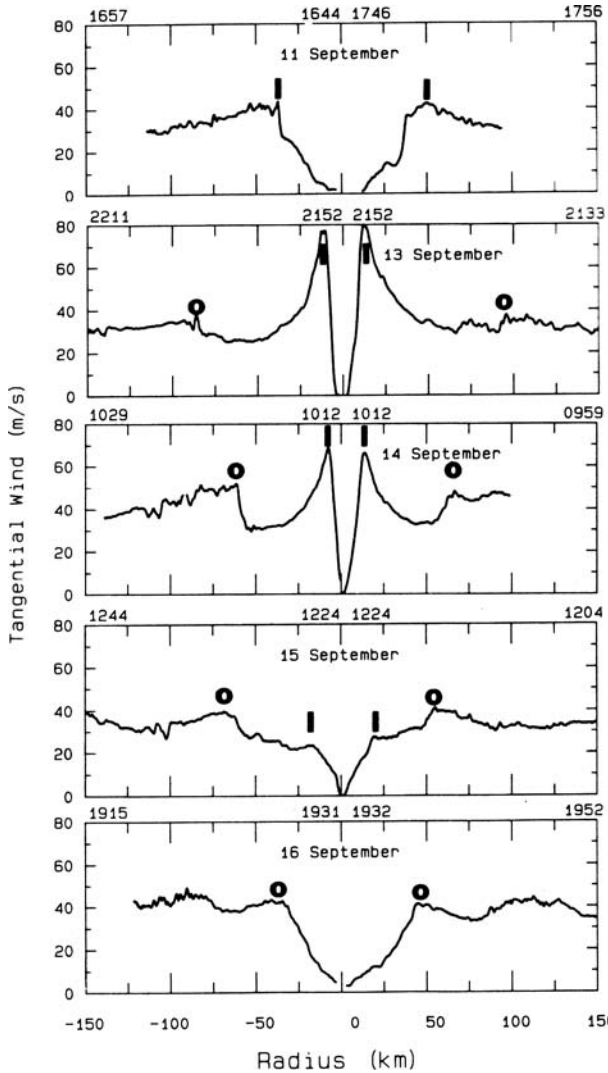

Fig. 1. Flight-level tangential wind speed from south to north traverses through the center of Hurricane Gilbert. Bold 'I' and 'O' denote the location of the inner and outer eyewall wind maximum, respectively. Times at the beginning and end of each radial pass are plotted at the top of the panels (refer to 1).

Finally, the outer eyewall replaced the inner eyewall and completed an eyewall replacement cycle (Fig. 1).

Several studies have devoted to understand mechanisms through which concentric eyewalls form. Willoughby *et al.*[10] and Willoughby[11] suggested

a symmetric instability that might contribute to the formation of the outer eyewall. They, however, could not develop a causal relation between the location of the outer eyewall and the instability. Montgomery and Kallenbach[3] implied that the TC concentric eyewalls could result from radially propagating linear vortex Rossby waves that are dynamically constrained near a critical radius. Since the development and propagation of the vortex Rossby waves are attributed to the TC basic state radial vorticity gradient, the vortex Rossby waves are confined near the radius of the maximum wind (RMW). Nong and Emanuel[4] studied the formation of the concentric eyewalls in an axisymmetric model. Their simulations showed that the secondary eyewall might result from a finite-amplitude WISHE instability, triggered by external forcing.

Black and Willoughby[1] noted that the outer eyewall formed during the TC weakening stage (Fig. 1). Shapiro and Willoughby[7] and Willoughby *et al.*[9] used a symmetric model (hereafter SW model) to diagnose the secondary circulation induced by a point heat source in balanced, axisymmetric vortices. For a heat source near RMW, a maximum of the tangential wind tendency lay just inside of RMW, so that the maximum wind propagated inward in response to the heating, which provided a plausible physical explanation for the contraction of the outer wind maximum. However, their simulations did not reproduce a double-peak structure. The fact that an outer eyewall forms during TC weakening stage suggests that a rapid decrease of convective heating may play a role in the formation of double eyewalls. Peng *et al.*[5] examined this idea by introducing a negative heat source in a simple TC model.

Theoretically, concentric eyewalls may be formed as two cyclonic vortices with different sizes and intensities interact without merging into a monopole.[2] The criteria for the concentric eyewall formation is that (1) the core vortex must be at least six times stronger in vorticity than the neighboring weaker vortex, (2) the neighboring vortex is larger in size than the core vortex, and (3) a separation distance is within three to four times of the core vortex radius. Note that in this scenario, a symmetric positive vortcity belt has been given initially. The interaction between the two vortices just redistributes the vorticity of the outer vortex. In this study, we present a different, wave–mean flow interaction scenario. We examine a new concentric eyewall formation scenario in which a core vortex interacts with an asymmetric perturbation that has a wave-like structure and zero symmetric vorticity component in the outer region. We will examine how the symmetric flow gains energy from the asymmetric perturbation in the

outer region, and how the second peak of the symmetric tangential wind is induced.

The outline of this paper is as follows. A brief description of the model and the experimental design is given in Sec. 2. Results from the nonlinear simulations are discussed in Sec. 3. Finally, a summary is given in Sec. 4.

2. Model Description

2.1. *The model*

To study the interaction between the core vortex and asymmetric perturbation, in particular to study how the asymmetry influences the symmetric flow, we construct a nonlinear barotropic model. The governing equations in a non-dimensional form on an f plane are given as the following:

$$\frac{\partial u}{\partial t} + u\frac{\partial u}{\partial x} + v\frac{\partial u}{\partial y} - v = -\frac{\partial \phi}{\partial x}, \tag{2.1a}$$

$$\frac{\partial v}{\partial t} + u\frac{\partial v}{\partial x} + v\frac{\partial v}{\partial y} + u = -\frac{\partial \phi}{\partial y}, \tag{2.1b}$$

$$-2J(u,v) - \zeta = -\nabla^2\phi, \tag{2.1c}$$

where $J(u,v) = \frac{\partial u}{\partial x}\frac{\partial v}{\partial y} - \frac{\partial v}{\partial x}\frac{\partial u}{\partial y}$ and $\zeta = \frac{\partial v}{\partial x} - \frac{\partial u}{\partial y}$, u and v are the horizontal wind velocity components; ϕ, the geopotential height, and ζ is the vorticity. The Coriolis parameter is $f = 5 \times 10^{-5}\,\mathrm{s}^{-1}$, and the characteristic value for time is $T = 1/f = 2 \times 10^4\,\mathrm{s}$. A non-dimensional time $t = 0.18$ corresponds to 1 h. The characteristic values for the velocity and horizontal length scales are $C = 50\,\mathrm{m/s}$ and $L = CT = 1000\,\mathrm{km}$, and the Rossby number equals 1 for the vortex.

The numerical solution technique employed is the fourth-order Runge–Kutta scheme with a time increment of 0.002. The Matsuno scheme[8] is applied to calculate the advection terms, and the second-order centered difference is used for the approximation of other space derivatives. A second-order diffusion is applied every 0.18 time with the non-dimensional coefficient being 1.4×10^{-6} to ensure the numerical stability. The model covers a 2×2 ($2000\,\mathrm{km} \times 2000\,\mathrm{km}$) area with a grid resolution of 0.002 in both x and y directions. The lateral boundary condition is radiative. All simulations are carried out for 24 h. Most of the results shown are up to 12 h during which the major axisymmetrization process occurs.

2.2. *Experiment design*

A core vortex is specified initially, which has a hurricane-like tangential wind profile (see Fig. 2) defined as follows:

$$V(r/R_{\max}) = V_{\max}\frac{2(r/R_{\max})}{1+(r/R_{\max})^2}, \tag{2.2}$$

where the maximum tangential wind $V_{\max} = 0.5(25\,\mathrm{m/s})$, and the radius of maximum wind $R_{\max} = 0.1(100\,\mathrm{km})$. The vorticity of the core vortex has a maximum at the center of the vortex (as seen in Fig. 1(c)) and decreases

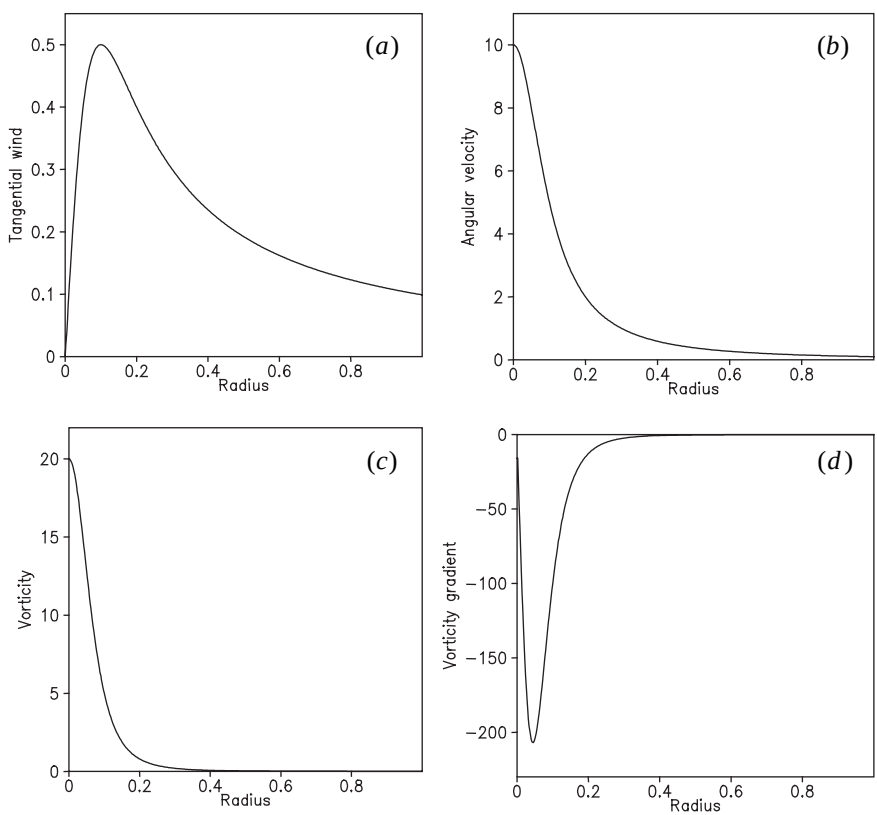

Fig. 2. Radial profiles of the hurricane-like vortex for nondimensional (a) tangential wind, (b) angular velocity, (c) vorticity, and (d) vorticity gradient. To obtain tangential wind in ms^{-1}, multiply by 50. To obtain angular velocity or vorticity in s^{-1}, multiply by 5×10^{-5}. To obtain vorticity gradient in $\mathrm{m}^{-1}\mathrm{s}^{-1}$, multiply by 5×10^{-11}. To obtain radial displacement in km, multiply by 1000.

monotonically with radius, with a maximum vorticity gradient located at $r = 0.044$ (Fig. 2(d)).

Different from the vortex–vortex interaction scenario in Kuo *et al.*,[2] we focus on the interaction between the asymmetric disturbances and symmetric core vortex flows. The initial asymmetry specified contains either a wavenumber 2 or a wavenumber 3 structure in the azimuthal direction. (To avoid the movement of the core vortex, a wavenumber-one asymmetry is not considered.) The initial asymmetry is prescribed by a vorticity perturbation with the following expression:

$$\varsigma' = 5 \exp\left[-\frac{1}{2}\left(\frac{r - R_{\mathrm{p}}}{\sigma}\right)^2\right] \cos(k\lambda), \tag{2.3}$$

where r is the radial distance; λ the azimuthal angle; k, the azimuthal wavenumber ($k = 2$ or $k = 3$) and the radial scale (or size) of the asymmetry $\sigma = 0.025$. The radial parameter R_{p} controls the position of the initial asymmetry.

To investigate how the initial asymmetry position might affect the formation of the second peak of the symmetric tangential wind, five experiments have been designed for the wavenumber 2 perturbations. In the first experiment the initial perturbation is placed at the radius of 0.2 ($R_{\mathrm{p}} = 0.2$, hereafter denoted as T20, see Fig. 3(a)). In the second

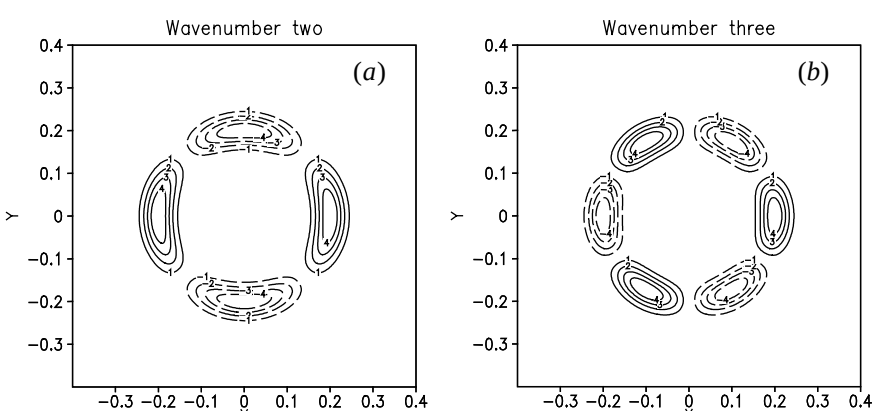

Fig. 3. The initial non-dimensional barotropic asymmetric vorticity with the maximum center located at the radius of 0.2 for (a) wavenumber 2 case T20 and (b) wavenumber 3 case H20. The contour interval is 1. To obtain vorticity in s^{-1}, multiply by 5×10^{-5}. To obtain radial displacement in km, multiply by 1000. Only the inner 400 km × 400 km model domain is shown.

experiment the initial asymmetry is placed at the radius of 0.25 ($R_\mathrm{p} = 0.25$, hereafter denoted as T25); the third one at the radius of 0.3 ($R_\mathrm{p} = 0.3$, denoted as T30); the fourth at the radius of 0.1 ($R_\mathrm{p} = 0.1$, denoted as T10); and the fifth at the radius of 0.15 ($R_\mathrm{p} = 0.15$, denoted as T15). The similar five sensitivity experiments with the wavenumber 3 disturbances are denoted as H20 ($R_\mathrm{p} = 0.2$), H25 ($R_\mathrm{p} = 0.25$), H30 ($R_\mathrm{p} = 0.3$), H10 ($R_\mathrm{p} = 0.1$), and H15 ($R_\mathrm{p} = 0.15$) respectively (Fig. 3(b)).

2.3. *Diagnosis method*

The diagnosis of the model output is carried out in a cylindrical coordinate system centered at the vortex center. Each model variable is decomposed into a symmetric and an asymmetric component, e.g. $u = \bar{u} + u'$, $v = \bar{v} + v'$, with a bar denoting the symmetric component and a prime the departure from the symmetric field.

The diagnostics for the energy budget is made with the following symmetric kinetic energy [KE, $\bar{K} = \frac{1}{2}(\bar{u}^2 + \bar{v}^2)$] equation:

$$\frac{\partial \bar{K}}{\partial t} = -\frac{\partial(r\bar{u}\bar{K})}{r\partial r} - \bar{u}\frac{\partial(r\overline{u'^2})}{r\partial r} - \bar{v}\frac{\partial(\overline{u'v'})}{\partial r} + \bar{u}\frac{\overline{v'^2}}{r} - \frac{2\bar{v}}{r}\overline{u'v'} - \bar{u}\frac{\partial\bar{\phi}}{\partial r}, \qquad (2.4)$$

where the first term on the right-hand side of (2.4) is the flux divergence of $\bar{K}$ by the symmetric radial flow, the sum of the second, third, fourth, and fifth terms represents the time change rate of symmetric KE due to wave–wave interactions, and the sixth term is the energy conversion from symmetric potential energy to symmetric kinetic energy. Note that the second-to-fifth terms on the right-hand side involve the interaction among the asymmetric perturbations and they are directly related to energy transfer between the asymmetry and the symmetry.

A Fourier analysis for vorticity is based on the following formula:

$$\zeta(r, \lambda, t) = \zeta_0(r, t) + \sum_{k=1}^{N}[\zeta_{kc}(r, t)\cos(k\lambda) + \zeta_{ks}(r, t)\sin(k\lambda)], \qquad (2.5)$$

where k is the azimuthal wavenumber, $\zeta_0(r, t)$, $\zeta_{kc}(r, t)$, and $\zeta_{ks}(r, t)$ are Fourier spectrum coefficients. The wavenumber spectrum of the first eight components are used to calculate the asymmetric component, and the Fourier asymmetric vorticity amplitude is defined by the following formula:

$$A_k(r, t) = \sqrt{\zeta_{kc}(r, t)^2 + \zeta_{ks}(r, t)^2}.$$

3. Results

We first diagnose the result from the wavenumber 2 perturbation simulations. Figure 4 shows the time evolution of the simulated symmetric tangential wind profile at a 3-h interval. As one can clearly see, a double-peak wind profile appears at hour 6. After that, the outer maximum continues to grow, while the inner peak experiences an oscillation in amplitude. For instance, at hour 9, there are two peaks in the symmetric tangential wind profile, with the inner one retaining bigger amplitude; at hour 12, the outer one has stronger amplitude.

A key question related to this double eyewall formation is how the outer wind peak is established. A notable feature is that the symmetric tangential wind in the outer region ($r > 0.15$) continues to grow while the wind in the inner region oscillates after initial rapid decay. These distinctive evolution features between the outer and inner regions are closely related to the energy transfer between the symmetric flow and the asymmetric perturbation, as shown in Fig. 5.

The diagnosis of the energy exchange between the symmetric and asymmetric components (the second-to-fifth terms on right-hand side of (2.4)) shows that outside of $r = 0.15$ there is always a positive energy

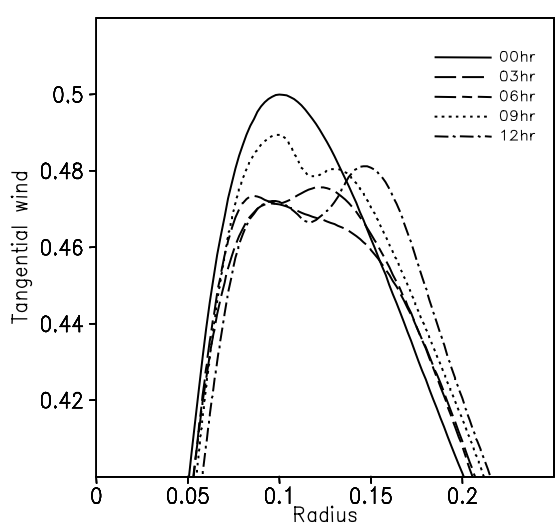

Fig. 4. The evolution of non-dimensional symmetric tangential wind profiles for case T20. To obtain tangential wind in ms^{-1}, multiply by 50. To obtain radial displacement in km, multiply by 1000.

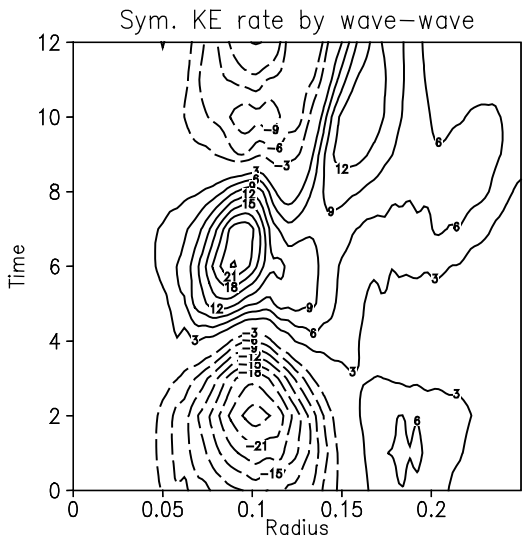

Fig. 5. The time–radius cross-section of the asymmetry-to-symmetric kinetic energy transfer rate (unit: $1.25 \times 10^{-4}\,\mathrm{m^2s^{-3}}$) in association with the wave–wave interactions in case T20. To obtain radial displacement in km, multiply by 1000. The time unit is hour.

transfer from the asymmetric perturbation to the symmetric flow, whereas inside of this radius there is oscillatory behavior in the energy transfer, that is, the symmetric flow gains energy from the asymmetry during hours 4–9 but loses energy into the asymmetry during hours 0–4 and 9–12. This is consistent with the time tendency of the symmetric tangential wind near RMW.

To understand the cause of the distinctive energy transfer behavior, we examine the asymmetric perturbation structure and its evolution characteristics. Figure 6 shows the time evolution of amplitude of the asymmetric perturbation. Note that in this numerical experiment (T20) the initial wavenumber 2 asymmetry is placed at the radius of 0.2. After time integration, a strong asymmetry is generated within the first four hours inside the radius of 0.1 where the absolute value of the symmetric vorticity gradient is the largest (Fig. 2(d)). The asymmetry amplitude in the outer region ($r > 0.15$), however, decreases gradually.

The horizontal pattern of the asymmetric perturbation reveals that the asymmetric vorticity field exhibits distinctive patterns during the different development stages. For example, at hour 1, the phase line connecting this newly generated asymmetry inside of RMW and the original outer

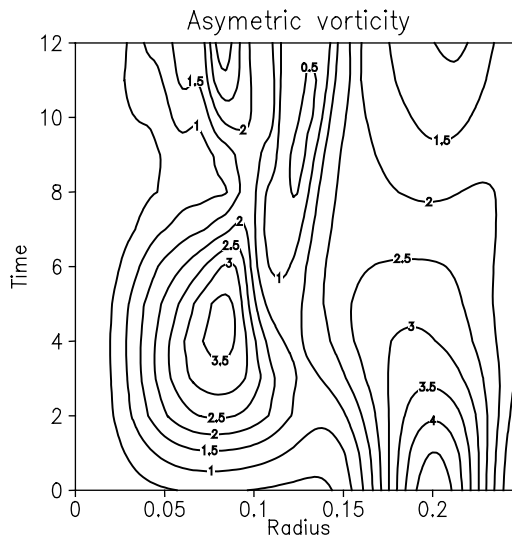

Fig. 6. The time–radius cross-section of the asymmetric vorticity amplitude (unit: $5 \times 10^{-5}\,\mathrm{s}^{-1}$) for case T20. To obtain radial displacement in km, multiply by 1000. The time unit is hour.

asymmetry shows an up-shear tilt (Fig. 7(a)) with respect to the rotation angular velocity of the core vortex (Fig. 2(b)). Because of this up-shear tilt, the symmetric flows transfer their energy to the asymmetric perturbations near $r = 0.1$ before hour 4 (Fig. 5), resulting in the weakening of the symmetric core vortex at hour 3 (Fig. 4). Because the symmetric angular velocity advects the inner asymmetry at a much faster rotation rate (see the angular velocity profile in Fig. 2(b)) than the outer asymmetry, the asymmetric vorticity shifts its phase to a down-shear tilt in the period of hours 4–9 (refer to Fig. 7(b)), so that the energy is transferred back to the symmetric flows (Fig. 5) and the asymmetric vorticity amplitude decreases during the period (Fig. 6). Thus, the symmetric tangential wind near the radius of 0.1 grows at the expense of the weakening of the asymmetry from hour 6 to hour 9 (Fig. 4). A new up-shear-tilting inner asymmetry is induced again after hour 9 (Figs. 6 and 7(c)). As a result, the symmetric flows transfer their energy to the asymmetric perturbations during hours 9–12, while the tangential wind at the inner core region weakens (Fig. 4).

In contrast, the symmetric flows always gain energy from the asymmetric disturbances in the outer region ($r > 0.15$) due to the steady down-shear phase tilt of the asymmetric disturbances (Fig. 7). This causes

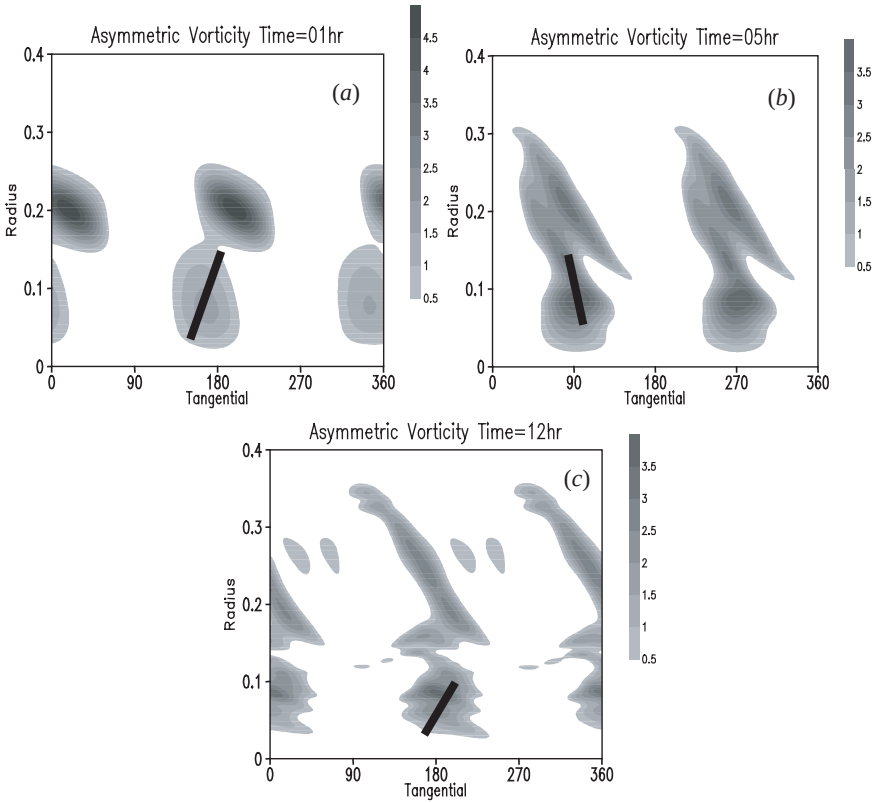

Fig. 7. The non-dimensional asymmetric vorticity pattern at time (a) 01 h, (b) 05 h and (c) 12 h for case T20. To obtain vorticity in s^{-1}, multiply by 5×10^{-5}. To obtain radial displacement in km, multiply by 1000.

the continuous intensification of the tangential wind in the outer region, leading to the formation of the second peak in the symmetric tangential wind profile.

To examine whether the aforementioned wind evolution characteristics change with different initial perturbations, we conduct a set of parallel experiments in which an initial wavenumber 3 asymmetry is introduced. Figure 8 shows the symmetric tangential wind evolution in case H20, where the initial asymmetric perturbation is placed at the radius of 0.2. Compared to case T20, a weaker asymmetry is generated near the radius of 0.1 (Fig. 9(a)). The comparison of symmetric kinetic energy change rates between the wavenumber 2 (T20) and wavenumber 3 (H20) perturbation

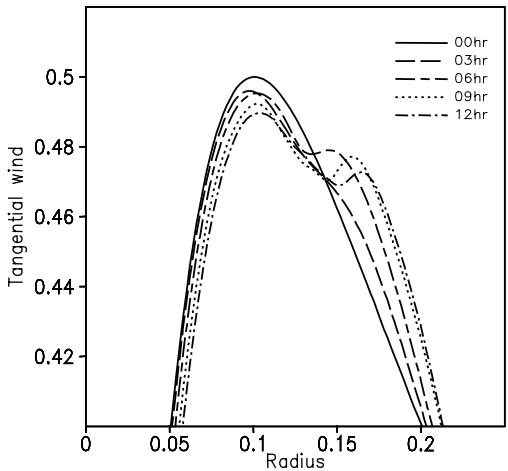

Fig. 8. The evolution of non-dimensional symmetric tangential wind profiles for wavenumber 3 initial disturbances in case H20. To obtain tangential wind in ms^{-1}, multiply by 50. To obtain radial displacement in km, multiply by 1000.

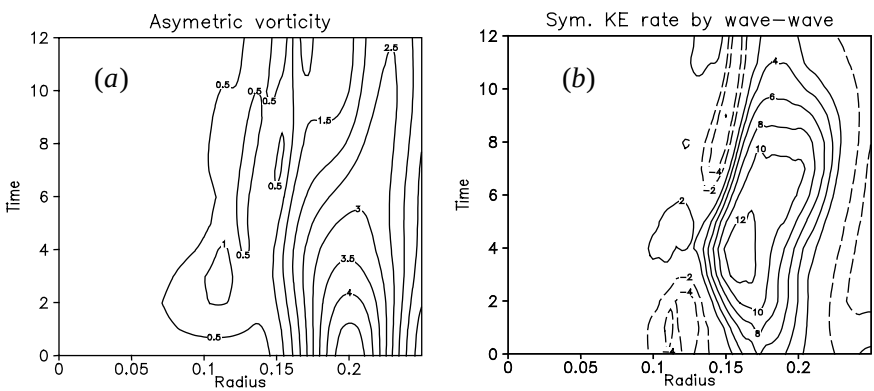

Fig. 9. The time–radius cross-section of (a) the asymmetric vorticity amplitude (unit: $5 \times 10^{-5}\,\mathrm{s}^{-1}$) and (b) the asymmetry-to-symmetry kinetic energy transfer rate (unit: $1.25 \times 10^{-4}\,\mathrm{m}^2\,\mathrm{s}^{-3}$) for wavenumber 3 initial disturbances in case H20. To obtain radial displacement in km, multiply by 1000. The time unit is hour.

experiments indicate that the energy exchange between the asymmetric and symmetric flows is weaker in the wavenumber 3 case. Nevertheless, a weak oscillation of the energy transfer is still present near the radius of 0.1, while in the outer region ($r > 0.15$) the wavenumber 3 initial disturbance can transfer more energy into the symmetric flows than the corresponding

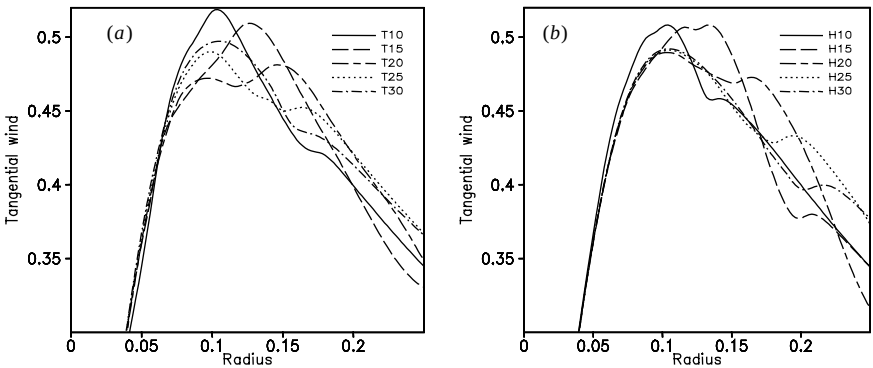

Fig. 10. The non-dimensional symmetric tangential wind profiles at 12 h for (a) wavenumber 2 and (b) wavenumber 3 initial disturbances. To obtain tangential wind in ms^{-1}, multiply by 50. To obtain radial displacement in km, multiply by 1000.

wavenumber 2 disturbance (Fig. 9(b)). It is again the down-shear tilt of the asymmetric perturbation and so induced asymmetry-to-symmetry energy transfer in the outer region that generate the second peak in the symmetric tangential wind profile (Fig. 8).

For the same-structure initial perturbation, is there a preferred radius location for the double eyewall formation? Our sensitivity experiments with the same wavenumber 2 or 3 initial perturbation but with different radial locations show that indeed there exists such an optimal radius. When the perturbation is placed more outward (i.e. T25, T30, H25, and H30) compared to the T20 and H20 experiments, the second peak in the symmetric tangential wind profile becomes weaker (Fig. 10), which means that the symmetric flows gain less energy from the asymmetric perturbations. On the other hand, when the initial asymmetry is placed more inward in T15 and T10 (H15 and H10), there is no obvious second-peak in the tangential wind profile. Thus, the sensitivity experiments above point out an optimal location near $r = 0.2$ (i.e. twice of RMW), where the initial asymmetry may generate the most significant double peaks in the symmetric tangential wind profile (Fig. 10).

4. Summary

The role of two-way interactions between a symmetric core vortex and an asymmetric disturbance in generating TC concentric eyewalls is examined

in a nonlinear barotropic model. The results show that when an asymmetric perturbation is placed at twice of RMW, an asymmetric disturbance develops in the inner core region, resulting in a weakening of the symmetric tangential wind. However, the symmetric flow gains energy from the asymmetric perturbations in the outer region, which induces the second peak of the symmetric tangential wind. This process is robust for both the wavenumber 2 and 3 perturbations, pointing out a new wave–mean flow interaction scenario for the double eyewall formation.

The numerical simulations illustrate that two distinctive symmetry–asymmetry interaction regimes in the inner and outer regions, respectively. While the symmetric tangential wind exhibits an oscillatory evolution in the inner region, it grows steadily in the outer region. This distinctive evolution feature is closely related to the asymmetric vorticity pattern, its up- or down-shear tilt, and so-induced symmetry-to-asymmetry or asymmetry-to-symmetry energy transfer.

Sensitivity numerical experiments indicate that there exists an optimal radius location (approximately near twice of the radius of the maximum wind) where the initial asymmetric disturbance may generate the most significant double-peak structure in the tangential wind profile. The optimal radius exists in both the wavenumber 2 and 3 experiments.

In the current study, a simple nonlinear barotropic model is used. Further studies with more sophisticated models are needed to validate the wave–mean flow interaction processes.

Acknowledgments

This work was supported by ONR grants N000140710145 and N000140210532, NRL subcontract N00173-06-1-G031, and National Natural Science Foundation of China under Grants 40205009 and 40333025. The International Pacific Research Center is partially sponsored by the Japan Agency for Marine-Earth Science and Technology (JAMSTEC). This is SOEST publication number 1234 and IPRC publication number 123.

References

1. M. L. Black and H. E. Willoughby, The concentric eyewall cycle of hurricane Gilbert, *Mon. Wea. Rev.* **120** (1992) 947–957.
2. H.-C. Kuo, L.-Y. Lin, C.-P. Chang and R. T. Williams, The formation of concentric vorticity structures in typhoons, *J. Atmos. Sci.* **61** (2004) 2722–2734.

3. M. T. Montgomery and R. J. Kallenbach, A theory for vortex Rossby-waves and its application to spriral bands and intensity changes in hurricanes, *Quart. J. Roy. Meteorol. Soc.* **123** (1997) 434–565.
4. S. Nong and K. A. Emanuel, A numerical study of the genesis of concentric eyewalls in hurricane, *Quart. J. Roy. Meteorol. Soc.* **129** (2003) 3323–3338.
5. J. Y. Peng, J. D. Jou, M. S. Peng, J. Fang and R. S. Wu, The formation of concentric eyewalls with heat sink in a simple tropical cyclone model, *Terrest. Atmos. Ocean. Sci.* **17** (2006) 111–128.
6. W. H. Schubert, J. J. Hack, P. L. Silva Dias and S. R. Fulton, Geostrophic adjustment in an axisymmetric vortex, *J. Atmos. Sci.* **37** (1980) 1461–4483.
7. L. J. Shapiro and H. E. Wiloughby, The response of balanced hurricanes to local sources of heat and momentum, *J. Atmos. Sci.* **39** (1982) 373–894.
8. T. L. Shen, Y. X. Tian, X. Z. Ge, W. S. Lu and D. H. Chen, *Numerical Weather Prediction* (Beijing Meteorology Press, 2003), pp. 145 (in Chinese).
9. H. E. Willoughby, J. A. Clos and M. G. Shoreibah, Concentric eye walls, secondary wind maxima, and the evolution of the hurricane vortex, *J. Atmos. Sci.* **39** (1982) 394–511.
10. H. E. Willoughby, H. L. Jin, St. J. Lord and J. M. Piotrowicz, Hurricane structure and evolution as simulated by an axisymmetric nonhydrostatic numerical model, *J. Atmos. Sci.* **41** (1984) 1161–9186.
11. H. E. Willoughby, The dynamics of the tropical cyclone core, *Aust. Met. Mag.* **36** (1988) 181–391.
12. H. E. Willoughby, J. M. Masters and C. W. Landsea, A record minimum sea level pressure observed in Hurricane Gilbert, *Mon. Wea. Rev.* **117** (1989) 2824–2828.